PCCP

PAPER

View Article Online
View Journal | View Issue

Cite this: *Phys. Chem. Chem. Phys.*, 2016, **18**, 21966

Effects of chemical substitution on the structural and optical properties of α-$Ag_{2-2x}Ni_xWO_4$ ($0 \leq x \leq 0.08$) solid solutions†

Wyllamanney da Silva Pereira,[a] Mateus Meneghetti Ferrer,[b] Gleice Botelho,[a] Lourdes Gracia,[c] Içamira Costa Nogueira,[d] Ivo Mateus Pinatti,[a] Ieda Lúcia Viana Rosa,[a] Felipe de Almeida La Porta,[e] Juan Andrés[c] and Elson Longo*[f]

Received 26th January 2016,
Accepted 27th June 2016

DOI: 10.1039/c6cp00575f

www.rsc.org/pccp

In this work, we investigated the effects of chemical substitution on the structural, electronic, and optical properties of α-$Ag_{2-2x}Ni_xWO_4$ ($0 \leq x \leq 0.08$) solid solutions prepared by a facile microwave-assisted hydrothermal method. The results showed that the increase of Ni concentration in α-Ag_2WO_4 microcrystals as a host matrix caused a morphological transformation and a shift of the electronic and optical properties. Based on first principles calculations and using Wulff's construction, particle shapes and their transformations in α-Ag_2WO_4 and α-$Ag_{2-2x}Ni_xWO_4$ can be affected by controlling the ratios of surface energy values between the different facets. In addition, theoretical calculations revealed that Ni substitution in α-Ag_2WO_4 is more favorable in the Ag_2 and Ag_4 positions, in which the local coordination of Ag atoms corresponds to clusters with coordination numbers of seven and four, respectively. This behavior could be related to the degree of medium-range structural disorder in α-$Ag_{2-2x}Ni_xWO_4$ crystals. The experimental results were correlated with theoretical simulations to achieve a deeper understanding of the relationship between morphology and properties. These results provide the basis for a rational design for the compositional modulation of structural and optical properties.

1. Introduction

Silver tungstate (Ag_2WO_4) based materials have been the subject of extensive research because of their excellent applications in different branches of science and technology, such as sensors, catalysts, bactericides, and photoluminescence.[1–18] Their excellent properties can be attributed to the flexibility of W and Ag in adopting the [WO_6] and [AgO_n] (n = 2, 4, 6, and 7) coordination modes, which can be linked further by other polyhedra to form three-dimensional structures.[2,9,19,20]

Notably, bulk Ag_2WO_4 can be found in three main phases: α-orthorhombic (with space group *Pn*2*n*), β-hexagonal (with space group *P*63/*m*), and γ-cubic (with space group *Fd*3*m*);[21] under ambient conditions, α-Ag_2WO_4 is the most stable polymorph.[8,21,22] In this context, well-defined α-Ag_2WO_4 crystals with various morphologies and sizes have been successfully synthesized using a variety of methods.[2,21,23] However, less attention has been devoted to α-Ag_2WO_4 crystals doped with different types of impurities.[24] Generally, successful doping requires substituent and host ions with comparable ionic radii and charges, allowing only a small disturbance in the crystal framework. This has been achieved in α-Ag_2WO_4, whose crystal structure is extremely flexible. The main purpose is to introduce additional bands and energy levels inside the intrinsic band gap, and thereby significantly change the electronic properties. Therefore, the rational control of the synthesis of solid solutions based on α-Ag_2WO_4 crystals has become a challenge, as it represents an important step in the development of new technologies based on α-Ag_2WO_4 materials.

Herein, for the first time, we report the facile synthesis of α-$Ag_{2-2x}Ni_xWO_4$ ($0 \leq x \leq 0.08$) microcrystal solid solutions by

[a] *INCTMN-UFSCar, Universidade Federal de São Carlos, P.O. Box 676, 13565-905 São Carlos, SP, Brazil. E-mail: wyllamanneysp@gmail.com, gleice.lorena@gmail.com, ivopinatti@hotmail.com, ilvrosa@ufscar.br*
[b] *Grupo de Modelagem e Simulação Molecular, INCTMN-UNESP, São Paulo State University, Bauru, SP CEP 17033-360, Brazil. E-mail: mmferrer@yahoo.com.br*
[c] *Departament de Química Física i Analítica, Universitat Jaume I (UJI), Castelló 12071, Spain. E-mail: lgracia@qfa.uji.es, andres@qfa.uji.es*
[d] *Instituto Federal de Educação, Ciência e Tecnologia do Maranhão (IFMA), PPGEM, São Luís, MA, Brazil. E-mail: isamiracosta@gmail.com*
[e] *Departamento de Química, Universidade Tecnológica Federal do Paraná (UTFPR), PO Box 3131, 86036–370, Londrina/PR, Brazil. E-mail: felipe_laporta@yahoo.com.br*
[f] *INCTMN-UNESP, Universidade Estadual Paulista, P.O. Box 355, CEP 14801-907 Araraquara, SP, Brazil. E-mail: elson.liec@gmail.com*

† Electronic supplementary information (ESI) available. See DOI: 10.1039/c6cp00575f

means of the microwave-assisted hydrothermal (MAH) method. We investigated the effect of chemical substitution on the structure, electronic, and optical properties, and a correlation between morphology and photoluminescence (PL) was found. Field-emission scanning electron microscopy (FE-SEM), transmission electron microscopy (TEM) X-ray diffraction (XRD) with Rietveld refinements, micro-Raman (MR) spectroscopy, Fourier transform infrared (FT-IR) spectroscopy, ultraviolet-visible (UV-vis) spectroscopy, and photoluminescence (PL) measurements were employed to characterize the samples. First-principles total-energy calculations were performed within the periodic density functional theory (DFT) framework using the Vienna *ab initio* simulation package (VASP). The paper is organized as follows: Sections 2 and 3 describe the experimental and theoretical details, respectively. Section 4 contains the results together with a discussion concerning the structure, morphology, and photoluminescence properties. Comprehensive and combined experimental and theoretical results are reported to understand the relationship between photoluminescence properties and order–disorder effects at short and medium ranges.

2. Experimental details

Synthesis of α-$Ag_{2-2x}Ni_xWO_4$ microcrystals

The starting precursors used in the synthesis of α-$Ag_{2-2x}Ni_xWO_4$ microcrystals were sodium tungstate dihydrate ($Na_2WO_4{\cdot}2H_2O$) (99.5%, Sigma-Aldrich), silver nitrate ($AgNO_3$) (99.8%, Sigma-Aldrich), and nickel(II) acetate tetrahydrate ($Ni(OCOCH_3)_2{\cdot}4H_2O$) (99.0%, Sigma-Aldrich). The α-Ag_2WO_4 microcrystals were synthesized at 140 °C for 1 h by using the MAH method. Briefly, 1 mmol of $Na_2WO_4{\cdot}2H_2O$ and 2 mmol of $AgNO_3$ were separately dissolved in plastic tubes with 50 mL of deionized water. Under vigorous magnetic stirring, the second solution was quickly added into the first solution. The resulting suspension (100 mL) was stirred for 10 min at room temperature, and subsequently transferred to a Teflon autoclave, which was placed in an adapted MAH system (2.45 GHz, maximum power of 1050 W). Finally, the resulting powder was washed with deionized water several times, and the collected precipitates were dried at 60 °C for 12 h.

The α-$Ag_{2-2x}Ni_xWO_4$ (x = 0.01, 0.02, 0.04 and 0.08) solid solutions were synthesized using 1 mmol of WO_4^{2-} ions, 1.98, 1.96, 1.92 and 1.84 mmol of Ag^+ ions and 0.02, 0.04, 0.08, and 0.16 mmol of Ni^{2+} ions, respectively. The remaining procedure was similar to that described for the synthesis of α-Ag_2WO_4.

Characterization of α-$Ag_{2-2x}Ni_xWO_4$ microcrystals

The obtained powders were structurally characterized by XRD using a Rigaku-DMax/2500PC with Cu Kα radiation (λ = 1.5406 Å) in the 2θ range from 10 to 70° with 0.2° min^{-1} and a step of 0.02. Phase analysis by the Rietveld method[25] was conducted using the General Structure Analysis System (GSAS) software with the EXPGUI graphical interface.[26] The Rietveld routine adopted a 2θ range from 10° to 110° with a scanning speed of 0.01° min^{-1}. The theoretical diffraction pattern was taken from the Inorganic Crystal Structure Database (ICSD) no. 4165,[27] which is based on the orthorhombic structure with the space group *Pn2n*. The refined parameters in the α-$Ag_{2-2x}Ni_xWO_4$ samples were the scale factor, background fitting with the Chebyschev polynomial of the first kind, shift lattice constants, profile half-width parameters, isotropic thermal parameters, lattice parameters, strain anisotropy factor, preferential orientation, and atomic functional positions. The peak profile function was modeled using a convolution of the Thompson–Cox–Hastings pseudo-Voigt (pV-TCH) function with the asymmetry function described by Finger.[28] FT-IR spectra were recorded in the range of 250–1000 cm^{-1}, using KBr pellets as a reference in a Bomen-Michelson spectrophotometer in transmittance mode (model MB-102). MR spectroscopy was conducted on a Horiba Jobin-Yvon (Japan) spectrometer coupled to a charge-coupled device detector and an argon-ion laser (Melles Griot, United States) operating at 514.5 nm with maximum power of 200 mW. The spectra were measured in the range of 25–1000 cm^{-1}. The morphologies were analyzed using a FEI (model Inspect F50) FE-SEM instrument operated at 5 kV. Elemental composition analysis was performed by means of EDX spectroscopy using a FEI microscope model Tecnai G2 F20. TEM analysis was performed on a CM200-Philips system and a JEOL JEM 2100F TEM/scanning TEM microscope operated at 200 kV.

In addition, the optical properties of the α-$Ag_{2-2x}Ni_xWO_4$ crystals at room temperature were analyzed by UV-vis and PL spectroscopies. UV-vis spectra were obtained using a Cary 5G spectrophotometer (Varian, USA) in diffuse reflection mode. PL spectra were measured using a Monospec 27 monochromator (Thermal Jarrel Ash, United States) coupled to a R446 photomultiplier (Hamamatsu Photonics, Japan). A krypton ion laser (Coherent Innova 200 K, United States) (λ = 350 nm) was used as the excitation source. The incident laser beam power on the sample was maintained at 15 mW. All experimental measurements were performed at room temperature.

Theoretical details

First-principles total-energy calculations were performed within the periodic DFT framework using the VASP code.[29–31] The Kohn–Sham equations were solved using the generalized gradient approximation in the Perdew–Burke–Ernzerhof (PBE) formulation for the electron exchange and correlation contribution to the total energy.[32,33] Owing to the well-known limitations of standard DFT in describing the electronic structure of "strongly correlated" compounds, a correction to the PBE wave functions was made (PBE+U), according to the formula of Dudarev *et al.*,[34] by including a repulsive on-site Coulomb interaction with the value of U = 6 eV for the Ag element, as in a previous study.[1] The conjugated gradient energy minimization method was used to obtain relaxed systems, which was accomplished by requiring the forces experienced by each atom to be smaller than 0.01 eV $Å^{-1}$. The electron–ion interaction was described by the projector-augmented-wave pseudopotentials.[35,36] The plane-wave expansion was truncated at the cut-off energy of 460 eV, and the Brillouin zones were sampled using a 4 × 4 × 4 special k-point mesh for the calculation of the equilibrium geometries and

electronic properties of the α-$Ag_{2-2x}Ni_xWO_4$ structures. The substitution of one Ni atom in Ag positions (Ag1, Ag2, Ag3, Ag4, Ag5, and Ag6) was explored for the four types of possible coordination modes. To evaluate the stability of substituted structures, we have directly compared the total energies of the Ni-substituted Ag_2WO_4.

The crystallite shapes could be determined by using the Wulff theorem and construction.[37–39] The procedure to obtain the complete set of morphologies, based on the variation of the surface energies, has been previously published by Andrés *et al.*[17,40]

3. Results and discussion

Structural order at long range

One of the first studies on the structural determination and refinement of Ag_2WO_4 was performed by Skarstad and Geller in 1975.[27] Today, the α-Ag_2WO_4 structure is well known,[27] and is based on a combination of experimental data and first principles calculations.[2,9,10] The geometry consists of different local polyhedra, such as distorted clusters with pentagonal bipyramid [AgO_7], octahedral, [AgO_6], tetrahedral [AgO_4], angular [AgO_2], and octahedral [WO_6] shapes, in which Ag–O and W–O bonds have weak interactions. Yang *et al.*[19] have recently confirmed this description.

Fig. 1 shows the XRD patterns of α-$Ag_{2-2x}Ni_xWO_4$ microcrystals synthesized at 140 °C for 1 h by the MAH method.

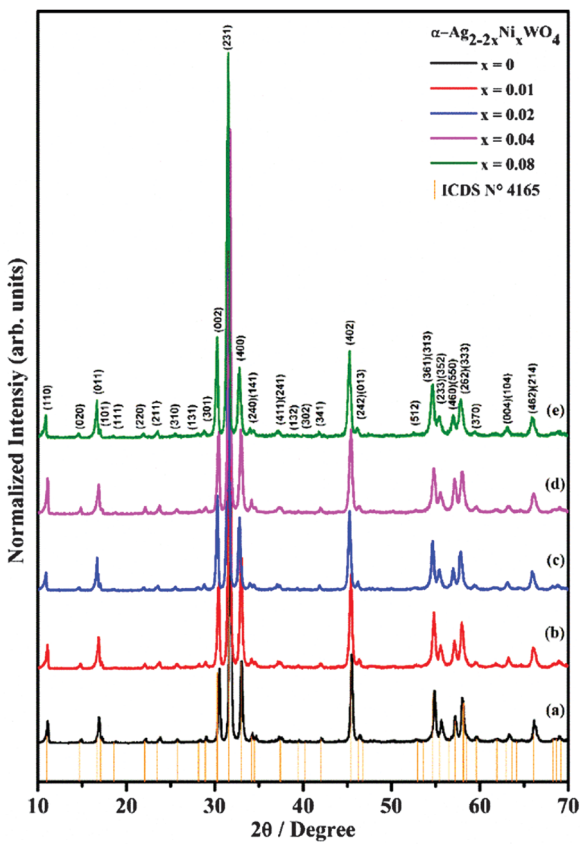

Fig. 1 XRD patterns of α-$Ag_{2-2x}Ni_xWO_4$ microcrystals with (a) x = 0, (b) x = 0.01, (c) x = 0.02, (d) x = 0.04, and (e) x = 0.08.

The analysis of the results showed that these crystals are monophasic and can be perfectly indexed to the orthorhombic structure with the space group *Pn*2*n*, and in good agreement with the ICSD no. 4165.[27]

The sharp and well-defined diffraction peaks indicated a high degree of structural order and crystallinity at long-range, proving the effectiveness of the MAH method employed in this work.

Fig. S1 (ESI†) illustrates the structural refinements of α-$Ag_{2-2x}Ni_xWO_4$ ($0 \leq x \leq 0.08$) microcrystals synthesized at 140 °C for 1 h by the MAH method, while Table S1 (ESI†) lists the small deviations of the statistical parameters (R_{wp}, R_{Bragg}, R_p, and χ^2), revealing the good quality of the structural refinements and numerical results. Analysis of the results shows that a solid solution is formed without the presence of secondary phases. The Rietveld refinement method also was used to calculate the lattice parameters, unit cell volumes and atomic coordinates of α-$Ag_{2-2x}Ni_xWO_4$ (with x = 0 and 0.08) microcrystals, thus analyzing the effects induced by the presence of Ni atoms. The values of the lattice parameters and unit cell volume are presented in Table 1. The substitution of Ag by Ni atoms provokes small changes in the lattice parameters and, consequently, in the unit cell volume. Moreover, variations in the atomic coordinates could be observed for the oxygen atoms, indicating the existence of possible structural distortions on the [WO_6] and [AgO_n] (n = 2, 4, 6, and 7) clusters (Tables S2 and S3, ESI†) according to the replacement of $[AgO_n]^{\times}$ by $[NiO_n]^{\bullet}$ complex clusters in the lattice.

The lattice parameters and atomic positions obtained from the Rietveld refinements were used as input data in the Visualization for Electronic and Structural Analysis program, version 3.2.1 for Windows,[41] to model the orthorhombic $Ag_{2-2x}Ni_xWO_4$ structure (Fig. 2). Occupancy sites of Ni atoms were investigated for α-$Ag_{2-2x}Ni_xWO_4$ (x = 0.08) solid solution employing Rietveld refinements, as listed in Fig. 2.

It is important to point out that Ag1 and Ag2 atoms form distorted pentagonal bipyramid [AgO_7] clusters. Ag3 atoms are located at the interior of these distorted octahedral [AgO_6] clusters; Ag4 and Ag5 atoms are coordinated by four O atoms to form distorted tetrahedral [AgO_4] clusters; and Ag6 atoms are bonded to two O atoms, forming angular [AgO_2] clusters.[1,2,11]

It was possible to estimate the distribution of Ni atoms at a concentration of 8 mol% in the atomic positions of Ag through Rietveld refinements. A distribution of Ni atoms at the available sites of each silver atom (Ag1 (4c), Ag2 (4c), Ag3 (2a), Ag4 (2a),

Table 1 Rietveld refinement details obtained for α-$Ag_{2-2x}Ni_xWO_4$ microcrystals by the increased replacement of the $[AgO_n]^{\times}$ by $[NiO_n]^{\bullet}$ complex cluster in the lattice

Samples α-$Ag_{2-2x}Ni_xWO_4$	Lattice parameters $\alpha = \beta = \gamma = 90°$			Cell volume (Å)^3
	a (Å)	b (Å)	c (Å)	
x = 0	10.89(64)	12.01(29)	5.88(69)	770.58(21)
x = 0.08	10.88(47)	12.02(77)	5.89(06)	771.19(4)
α-Ag_2WO_4 (ICSD 4165)	10.89(2)	12.03(2)	5.92(2)	775.56

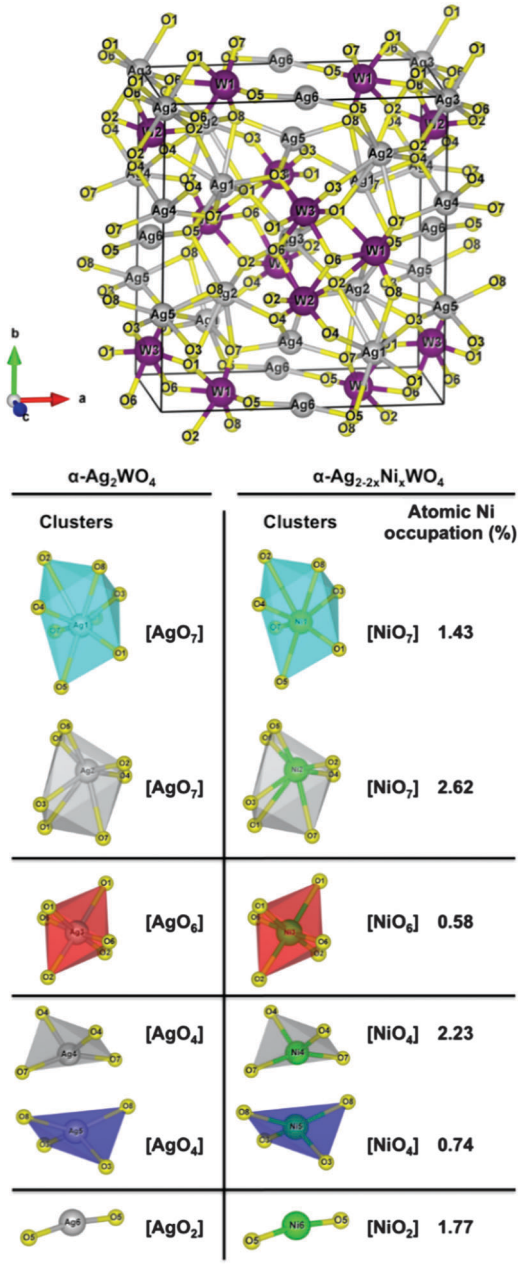

Fig. 2 Schematic representation of α-Ag_2WO_4 and α-$Ag_{2-2x}Ni_xWO_4$ structures, respectively. The results of the Ni atomic occupation obtained from Rietveld refinement for different sites belonging to the Ag clusters [AgO_n] (n = 2, 4, 6, and 7) are also shown.

Ag5 (2a), Ag6 (2b)) was carried out, showing that the Ni atoms are more present in pentagonal bipyramid [NiO_7] and tetrahedral [NiO_4] clusters (Fig. 2). 1 mol%, 2 mol% and 4 mol% Ni concentrations are too low to correctly estimate the substitution process of these ions within the crystal lattice.

First principles calculations were used to confirm the experimental results, and to evaluate the favorable occupation sites of Ni atoms. The substitution of a Ni atom at six different Ag positions (Ag1, Ag2, Ag3, Ag4, Ag5, and Ag6) was calculated with a concomitant Ag vacancy to compensate the positive charge balance. The theoretical results indicated that 6.25% Ni could

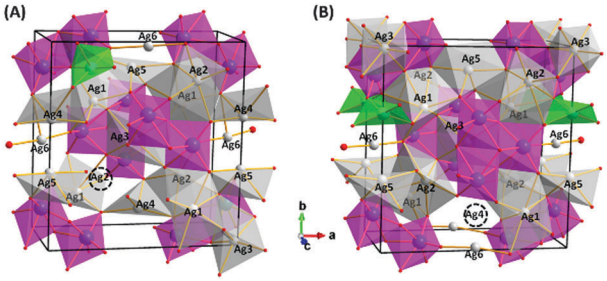

Fig. 3 Theoretical representation of α-$Ag_{2-2x}Ni_xWO_4$ with x = 6.25% distributed in (A) Ag2 and (B) Ag4 positions. The vacancy is depicted as the dashed circle.

be distributed in both the Ag2 and Ag4 positions, confirming them as the most favorable substitution sites, in good agreement with the Rietveld results. The Ni substitution in the Ag2 position was 0.3 eV more stable than that in the Ag4 position; the Ni substitutions in the remaining Ag sites appeared more difficult, owing to a difference in energy of 1.3 eV, compared with the Ag2 position. The α-$Ag_{2-2x}Ni_xWO_4$ geometry showing the Ni addition and vacancy positions is depicted in Fig. 3. When an Ag2 atom is replaced by a Ni atom, the coordination changes from seven to five, with four similar distances in the range 1.89–1.99 Å and a larger distance of 2.828 Å; in this case, a vacancy of one Ag2 atom is the most stable arrangement, as shown in Fig. 3(A). However, in the case of a Ni atom replacing an Ag4 atom, the 4-fold coordination is maintained with two sets of distances of 1.900 Å and 1.949 Å; in this case a vacancy of another Ag4 takes place, as shown in Fig. 3(B). It is worth noting that after the corresponding tests, the most stable placement for the vacancy is the same type of site as the one occupied by Ni. In the two cases, Ni substitution favors the formation of more symmetric and compact polyhedra with shorter Ni–O distances compared to Ag–O distances in their respective sites.

Structural order at short range

Raman and FT-IR spectroscopies are crucial to explore the structural short-range organization.

Fig. 4(A) shows the MR spectra of the α-$Ag_{2-2x}Ni_xWO_4$ microcrystals ($0 \leq x \leq 0.08$). In these spectra, the presence of 17 Raman-active vibrational modes at room temperature was observed, in good agreement with other studies.[10,11,42] In particular, the Raman active mode detected at $\sim$60 cm^{-1} (Fig. 4(A)) in the spectrum of the α-$Ag_{2-2x}Ni_xWO_4$ ($0 \leq x \leq 0.08$) microcrystals could be assigned to the external phonons for the motion of Ag^+ ions. The most intense peak centered at 883 cm^{-1} was associated with the vibrations of the symmetrical stretch of the ($\leftarrow O \leftarrow W \rightarrow O \rightarrow$) bond in the [$WO_6$] cluster.[10,11,42]

Fig. 4(B) shows the FT-IR spectra of α-$Ag_{2-2x}Ni_xWO_4$ ($0 \leq x \leq 0.08$) crystals. While the FT-IR spectra of the α-Ag_2WO_4 microcrystals showed only four active modes, α-$Ag_{2-2x}Ni_xWO_4$ ($0.01 \leq x \leq 0.08$) solid solutions exhibited 13 active modes. Of these 13 modes, 11 are related to Ag_2WO_4 and 2 modes correspond to the Ni–O bond. These results were in agreement with the findings reported in the literature.[43–46]

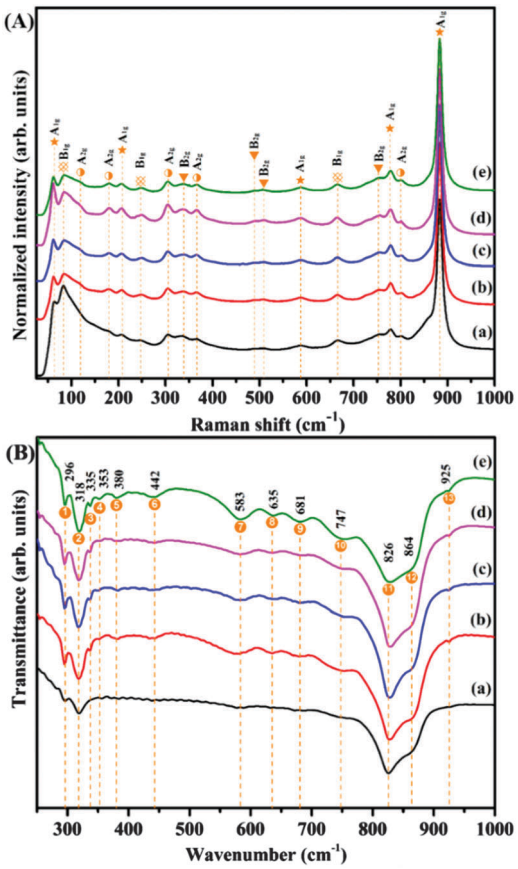

Fig. 4 (A) MR and (B) FT-IR spectra of α-$Ag_{2-2x}Ni_xWO_4$ microcrystals with (a) $x = 0$ (b) $x = 0.01$, (c) $x = 0.02$, (d) $x = 0.04$, and (e) $x = 0.08$.

The two intense absorption bands at 826 cm^{-1} and 864 cm^{-1} were assigned to asymmetric vibrations of the (←O←W←O←) and (→O→W→O→) bonds within the distorted [WO_6] clusters.[2,44] The internal vibrational mode at 318 cm^{-1} was related to the symmetric bending vibration of O–W–O in the distorted [WO_6] clusters, while the vibrational mode at 296 cm^{-1} corresponded to the twisting motion of [WO_6].[11] The band at 635 cm^{-1} indicates bridging oxygen atoms in the W_2O_2 asymmetric stretching mode.[45] Active modes at 747 cm^{-1} and 925 cm^{-1} were assigned to the vibrations of the O–W–O bonds, while the mode at 681 cm^{-1} corresponds to W–O–W bonds.[44,47] The absorption bands at 353 cm^{-1} and 442 cm^{-1} detected in the infrared spectra of solid solutions were due to the vibrations of the Ni–O bond,[44–46] indicating the replacement of Ag atoms by Ni atoms.

The presence of defined Raman and FT-IR active modes in the spectra revealed that all samples were structurally ordered in the short range. Notably, more defined spectra were observed for the $Ag_{2-2x}Ni_xWO_4$ ($0.01 \leq x \leq 0.08$) solid solutions (Fig. 4), likely due to a decreased concentration of structural defects upon insertion of Ni atoms in the Ag_2WO_4 lattice. However, independent of the Ni concentration, these samples are not free of structural defects, as demonstrated by photoluminescence studies. In addition, the spectra of Ni-substituted crystals seem to be more defined that could be attributed to intensity changes.

Morphological aspects

An efficient control of the size, shape, composition, structure, and surface chemistry of materials enables the modification of the physical and chemical properties.[17,48–51]

Fig. 5 shows FE-SEM images of α-$Ag_{2-2x}Ni_xWO_4$ ($0 \leq x \leq 0.08$) microcrystals. All samples have an agglomerative nature with a

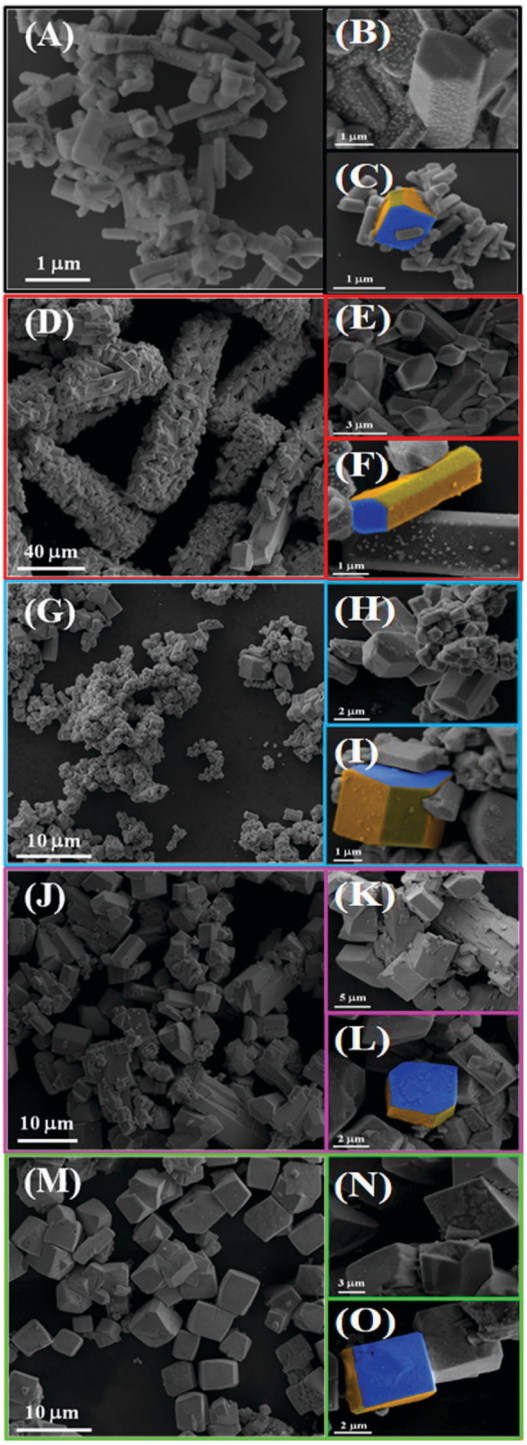

Fig. 5 FE-SEM images of α-$Ag_{2-2x}Ni_xWO_4$ microcrystals with: (A–C) $x = 0$, (D–F) $x = 0.01$, (G–I) $x = 0.02$, (J–L) $x = 0.04$, and (M–O) $x = 0.08$.

polydisperse size distribution and shape (Fig. S2 in ESI†). The presence of agglomerated particles, having surface defects, may arise as a result of Ostwald ripening.[52] α-Ag_2WO_4 microcrystals have a hexagonal rod-like elongated shape, as verified in Fig. 5(A–C). According to Roca *et al.*,[17] α-Ag_2WO_4 crystals have preferential growth along the [010] direction. Substitution of 1 mol% of Ag by Ni atoms resulted in microcrystals with hexagonal faces agglomerated more readily, forming rod-shaped superstructures (Fig. 5(D and E)).

Previous studies have shown the development of metallic Ag nanoparticles on the surface of α-Ag_2WO_4 crystals driven by a beam of accelerated electrons from an electron microscope under high vacuum.[1,9–12] For the sample with x = 0.01, the growth of irregular metallic Ag nanoparticles on the surface of α-$Ag_{2-2x}Ni_xWO_4$ microcrystals was also observed (Fig. 5(F)).

Fig. 5(G–I) show that 2 mol% of Ni modified the microcrystal shapes, favoring the formation of hexagonal microparticles. Ni atoms were likely to inhibit the crystal growth in the [010] direction.[17] Fig. 5(J–L) show the α-$Ag_{2-2x}Ni_xWO_4$ (x = 0.04) solid solution, which exhibited a more faceted hexagonal-platelet-like shape. Finally, 8 mol% of Ni caused a pronounced change in microcrystal shapes, leading to the formation of faceted micro-pseudocubes (Fig. 5(M and N)). In this case, higher concentrations of Ni added in the α-$Ag_{2-2x}Ni_xWO_4$ structure are able to promote the growth of the (010) surface (displacement in the [010] direction) and yield its reduction (Fig. 5(O)).

The Wulff construction of the ideal structure, according to the surface energies previously obtained by our group,[17,40] and the morphology modulations due to the energy ratios are presented in Fig. 6. Calculations of the surface energy of different Ni substituted facets are performed and tabulated in Table S4 (ESI†), maintaining the ratio of surface energy between facets, compared to the pure system.

According to our previous simulation, Ag_2WO_4 under vacuum exhibits a cubic morphology. On this basis, considering the Wulff theorem, it is possible to change the surface energy ratios to find the experimental morphologies. This is a simple method to evaluate the energy ratios by circumventing all the real variables of an experimental system. As a result, α-$Ag_{2-2x}Ni_xWO_4$ samples with x equal to 0 (Fig. 5(A–C)), 0.01 (Fig. 5(D–F)), and 0.02 (Fig. 5(G–I)) were composed mainly of particles with the same morphologies obtained theoretically with (110) E_{surf} = 0.20 J m^{-2} and (110) E_{surf} = 0.16 J m^{-2}/(011) E_{surf} = 0.40 J m^{-2} (Fig. 6). The α-$Ag_{2-2x}Ni_xWO_4$ sample with x = 0.04 and 0.08 (Fig. 5(J–L) and (M–O), respectively), although consisting of a few particles with morphologies similar to those of the previous samples, mainly showed cubic particles as the ideal system, and also (110) E_{surf} = 0.26 J m^{-2}/(011) E_{surf} = 0.37–0.40 J m^{-2}/(101) E_{surf} = 0.53, as shown in Fig. 6. Another important factor to consider is the oscillation of the width observed in and between the samples.

Fig. 6 shows one of the morphologies from a different angle, and the changes caused by the (001) E_{surf} variation. The instability of the (001) surface in this model resulted in more elongated particles. Therefore, the oscillation of the elongation size in the experimental system produced evidence that the (001) surface had a considerable energy amplitude.

Fig. 7 shows a schematic representation of the main stages involved in the synthesis and growth mechanisms of α-$Ag_{2-2x}Ni_xWO_4$ microcrystals based on the FE-SEM micrographs.

Under hydrothermal conditions, the viscosity of water decreases, and the mobility of ions and dissolved molecules is then enhanced. The microwave energy acts directly on the rotation barrier of

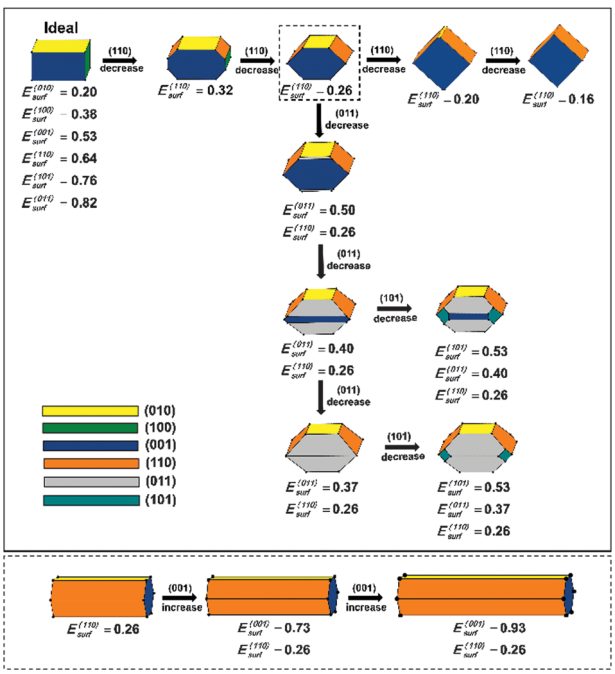

Fig. 6 Map of morphologies of α-Ag_2WO_4 with (010), (100), (001) (110), (101), and (011) crystal planes. Surface energy is expressed in J m^{-2}.

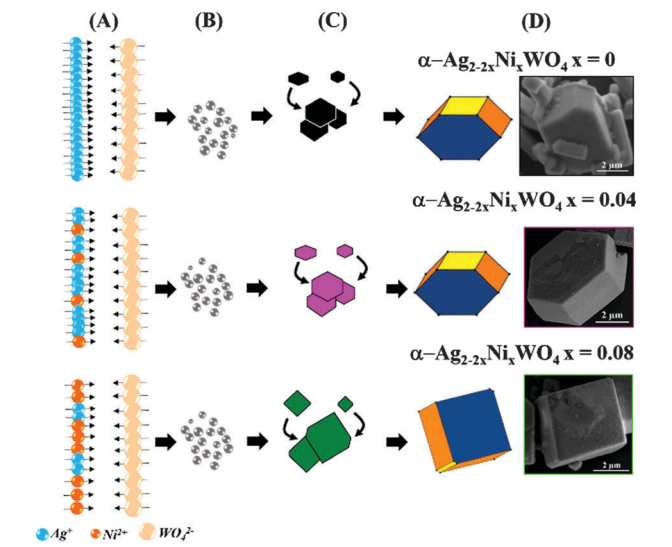

Fig. 7 Schematic illustration of the proposed growth mechanism leading to the formation of α-$Ag_{2-2x}Ni_xWO_4$ microcrystals: (A) electrostatic attraction of Ag^+/Ni^{2+} and WO_2^{4-} ions in solution and the possible interactions; (B) formation of small nuclei; (C) aggregation of small particles *via* microwave irradiation and growth *via* OR; (D) final crystal shapes.

the water molecules, forcing the kinetic crystallization of the particles.[48,53] Thus, the hydration energy is overcome by the strong electrostatic attraction between the Ag^{+}/Ni^{2+} and WO_4^{2-} ions, hence forming primary particles (Fig. 7(A and B)). As these nuclei have free rotation, they collide at random and rearrange in relation to each other through Brownian motion,[54] resulting in the formation of microcrystals with hexagonal faces. Moreover, microwave irradiation can promote the formation of aggregated particles under hydrothermal conditions.[55,56] When the system reached equilibrium between the solubility and precipitation processes, Ostwald ripening (OR) can occur[52] (Fig. 7(C and D)). In this mechanism, larger particles were formed by dissolving smaller particles, owing to the energy difference between them, reflected on their solubilities by the Gibbs–Thomson law.[57] In particular, the irregularities and surface defects found in α-$Ag_{2-2x}Ni_xWO_4$ microcrystals can indicate the predominance of this type of crystal growth (Fig. 7(D)).

The TEM images of the α-Ag_2WO_4 and α-$Ag_{2-2x}Ni_xWO_4$ (x = 0.08) microcrystals confirmed the dynamic aggregation of primary particles in various processes in different directions (Fig. S3 in the ESI†). The selected area of electron diffraction images in the insets of Fig. S3(A and B) (ESI†) for α-Ag_2WO_4 and α-$Ag_{2-2x}Ni_xWO_4$ (x = 0.08), respectively, reveal a common pattern of polycrystalline material electron diffraction.

Structural order at medium range

The optical band gap energy (E_{gap}) was calculated by the Wood and Tauc method,[58] using the function proposed by Kubelka and Munk.[59] According to Tang *et al.*[13] and Kim *et al.*,[60] the Ag_2WO_4 crystals exhibited an optical absorption spectrum governed by direct electronic transitions between the valence and conduction bands.

Theoretical results have shown that the symmetry breaking process, or the effect of the order–disorder transition in the structure of various semiconductors, is a necessary condition for the existence of intermediary energy levels within the forbidden band gap.[61] These structural changes are related to the charge polarizations at short and medium ranges ($[WO_6]$–$[WO_6]$, $[AgO_n]$–$[AgO_n]$, or $[WO_6]$–$[AgO_n]$ complex clusters), which can be manifestations of quantum confinement. The key point of quantum confinement is the presence of discrete energy levels within the band gap, which are not possible for a periodic crystal at long, medium, and short ranges.

Fig. S4 (ESI†) shows the UV-vis spectra of all samples. The E_{gap} estimated values (3.19 eV to 3.12 eV) could be associated with distortions in the local lattice ($\cdots[AgO_n]$–$[WO_6]$–$[NiO_n]\cdots$ with n = 2, 4, 6, or 7) as well as the intrinsic surface states and interfaces that produce electronic levels located within the band gap.

The computed band value for pure Ag_2WO_4 was 2.0 eV.[1] When 6.25% of Ag was replaced by Ni, reduction to 0.81 eV and 1.29 eV was observed for the Ni substitutions of Ag2 and Ag4, respectively, as shown in Fig. S5 (ESI†). Notably, there was a greater decrease in the band gap when a major local distortion was caused by the Ni replacement (for Ag2, a change in the coordination occurred), in agreement with the experimental results.

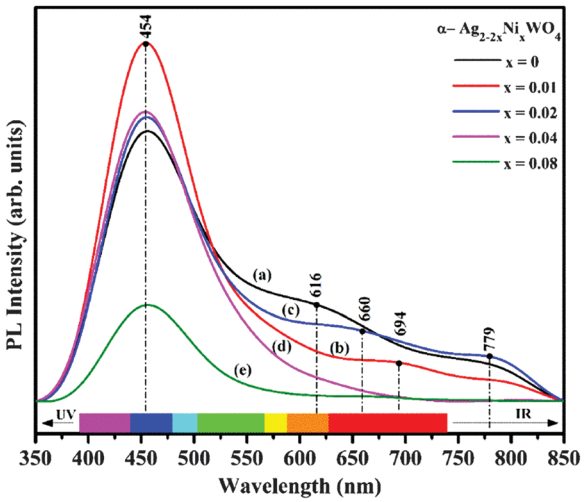

Fig. 8 PL spectra of α-$Ag_{2-2x}Ni_xWO_4$ microcrystals with (a) x = 0, (b) x = 0.01, (c) x = 0.02, (d) x = 0.04, and (e) x = 0.08.

In addition, calculations using this type of function typically underestimate the band gap values, typical for DFT calculations.[1,62]

PL measurements were performed to provide a better understanding of the structural and electronic order–disorder effects at a medium distance in the α-$Ag_{2-2x}Ni_xWO_4$ microcrystals. The PL spectra of α-$Ag_{2-2x}Ni_xWO_4$ microcrystals revealed an intense blue luminescence emission (Fig. 8), with a broadband profile and a maximum emission of 454 nm located in the blue region. In the literature, the PL emission spectra of tungstates are frequently decomposed into violet, blue, green, yellow, orange, and red light components,[63] with some controversial interpretations with regard to the blue and green maximum PL emissions.[64–67]

In general, it is assumed that the emission spectra of metal tungstates are associated with the charge-transfer transitions within the $[WO_4]$ complexes,[68–70] or due to oxygen vacancies such as $[WO_3{\cdot}V_o]$.[64,71] The emission peaks detected at lower energies were related to deep level defects due to distortions in the lattice modifier clusters $[AgO_n]$ (n = 2, 4, 6, and 7).[11] This behavior can also be observed in the PL spectra of other complex metal oxides involving different Ag clusters.[6,10,55,56]

In the present materials, $Ag_{2-2x}Ni_xWO_4$ ($0 \leq x \leq 0.08$), the PL emissions are in the green-orange region due to the substitution process of Ag by Ni atoms, owing to the formation of new $[NiO_n]$ clusters in the Ag_2WO_4 lattice, which were responsible for the different distributions and organizations of intermediate energy levels within the forbidden band gap. To better understand the influence of the different concentrations of Ni on the optical properties of the α-$Ag_{2-2x}Ni_xWO_4$ solid solution, the individual contributions of each component of the PL spectra were decomposed using the Voigt function modeled in the PeakFit program (version 4.05), including the peak positions and corresponding areas, as shown in Fig. 9.

The literature[63] reports that deep holes are responsible for the green, yellow, orange, and red PL emissions at room temperature, while shallow holes cause the violet and blue emissions. Deconvolution of the PL spectrum of α-Ag_2WO_4,

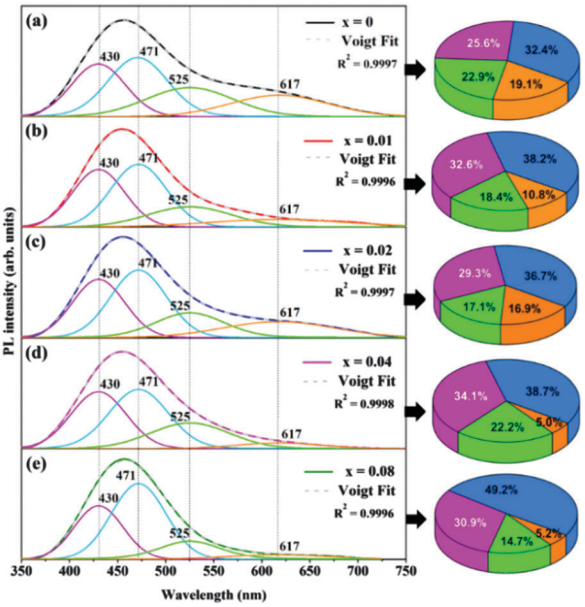

Fig. 9 Deconvolution of PL spectra of α-$Ag_{2-2x}Ni_xWO_4$ microcrystals with: (a) x = 0, (b) x = 0.01, (c) x = 0.02, (d) x = 0.04, and (e) x = 0.08. Insets in (a–e) show the area percentage of each color component corresponding to the emission peak.

shown in Fig. 9(a), suggests that the configuration of the levels within the band gap favored both types of defects, as the sum of the percentages of the PL emission areas of the components corresponding to shallow structural defects (emission of violet and blue light) and deep holes (green and orange light emission) are similar.

The cluster-to-cluster charge-transfer (CCCT) in a crystal is characterized by excitations involving electronic transitions from one cluster to another.[56] The $[WO_6]_o^\times - [WO_6]_d^\times$ and $[AgO_n]_o^\times - [AgO_n]_d^\times$ (n = 2, 4, 6, or 7; o = ordered; d = distorted) clusters may have arisen from structural distortions within the α-Ag_2WO_4 lattice, and the electronic transfer can occur between them. Therefore, the $[WO_6]_o - [WO_6]_d$ and $[AgO_n]_o - [AgO_n]_d$ clusters presented intrinsic defects, which were linked to the effects of the order–disorder transitions in the electronic structure, surfaces, and interfaces, and are commonly found in materials with a Scheelite-type structure and synthesized using the MAH method.[63,72–75]

The PL properties of Ag_2WO_4 crystals could be explained considering the density of structural defects responsible for changes in the configuration of the intermediate states within the band gap.[2] α-Ag_2WO_4 can generate electron–hole pairs (e'–$h^\bullet$) before reaching the photon energy system. This phenomenon is caused by structural distortions of $[WO_6]_d/[AgO_n]_d$ with n = 2, 4, 6, and 7 (intrinsic defects of the array); these defects are able to polarize the lattice and lead to electronic transitions between $[WO_6]_d^\times/[AgO_n]_d^\times$ (disordered neutral clusters) and $[WO_6]_o^\times/[AgO_n]_o^\times$ (ordered neutral clusters). When the photon energy (λ = 350 nm) is absorbed by the crystals, the processes represented by the notation of Kröger–Vink[76] may occur (eqn (1) to (4)):

$$[WO_6]_d^\times + [WO_6]_o^\times \xrightarrow{h\nu} [WO_6]_d^\bullet + [WO_6]_o' \quad (1)$$

$$[AgO_n]_d^\times + [AgO_n]_o^\times \xrightarrow{h\nu} [AgO_n]_d^\bullet + [AgO_n]_o' \quad (2)$$

$$[WO_6]_d^\times + [AgO_n]_o^\times \xrightarrow{h\nu} [WO_6]_d^\bullet + [AgO_n]_o' \quad (3)$$

$$[AgO_n]_d^\times + [WO_6]_o^\times \xrightarrow{h\nu} [AgO_n]_d^\bullet + [WO_6]_o' \quad (4)$$

In general, the Ni atoms in α-$Ag_{2-2x}Ni_xWO_4$ solid solutions lead to a more pronounced generation of shallow defects rather than deep holes, favoring the high-energy emissions (Fig. 9). The substitution of Ag by Ni atoms provokes the formation of more ordered clusters in the crystal lattice of the α-$Ag_{2-2x}Ni_xWO_4$ ($0.01 \leq x \leq 0.08$) solid solutions. In the case of α-$Ag_{2-2x}Ni_xWO_4$ (x = 0.04 and x = 0.08), the increased presence of $[NiO_n]^\bullet$ clusters seems to suppress PL emissions, as they interacted with the $[WO_6]_o' / [AgO_n]_o'$ clusters, neutralizing them and contributing to the structural reorganization, as described by eqn (5) and (6).

$$[NiO_n]_o^\bullet + [WO_6]_o' \xrightarrow{h\nu} [NiO_n]_o^\times + [WO_6]_o^\times \quad (5)$$

$$[NiO_n]_o^\bullet + [AgO_n]_o' \xrightarrow{h\nu} [NiO_n]_o^\times + [AgO_n]_o^\times \quad (6)$$

In eqn (1) to (6), the superscript x indicates neutral clusters, $^\bullet$ indicates the cluster with one hole ($h^\bullet$), $'$ indicates the cluster with one electron (e'), and n equals 2, 4, 6, or 7 for the $[AgO_n]$ cluster, while for the $[NiO_n]$ cluster n is more likely to assume the values 4 and 7, considering the results of the Rietveld refinement.

In addition to the distortions in the $[WO_6]$ and $[AgO_n]$ clusters (n = 2, 4, 6, and 7), the PL of α-$Ag_{2-2x}Ni_xWO_4$ microcrystals appeared to be associated with alterations in the morphology and aggregation of the particles. Then, the morphological aspects were able to dislocate the crystal lattice planes as well as adjacent particles in the aggregates, producing different density defects in the crystals.[56] In addition, changes in the shape and size of the particles can be considered as additional key factors responsible for the variations of the PL emission profiles. In this context, we can define the PL property as an average contribution of the surfaces and the core of the crystal, including all the defects. Therefore, it is possible to associate the changes in PL observed for the samples having different amounts of Ni with our morphology study described above (see also Fig. 5 and 6). Different exposed surfaces contribute as different PL sources, directly or indirectly. As concluded previously, the addition and increase of Ni content as a substituent in the system favored the formation of particles with a greater degree of symmetry, and consequently with a smaller quantity of different exposed surfaces. The correlation between FE-SEM images and theoretical morphologies is highlighted in Fig. S6 (ESI†). These results are in agreement with the narrowing of the PL band and also the decrease of deep defects, due to better homogenization of the PL sources.

4. Conclusions

In summary, α-$Ag_{2-2x}Ni_xWO_4$ ($0 \leq x \leq 0.08$) solid solution crystals were successfully grown by the MAH method, and the introduction of Ni^{2+} ions to simultaneously control the crystal structure, morphology, and optical properties was explored for the first time. FE-SEM, XRD, MR, FT-IR, TEM, UV-vis, and PL measurements were extensively employed to investigate the differences in the coordination environments and specific structural arrangements upon replacement of $[AgO_n]^{\times}$ by the $[NiO_n]^{\bullet}$ complex cluster. Theoretically, the presence of 6.25% of Ni that can be distributed at both Ag2 and Ag4 positions, which form clusters with coordination seven and four, respectively, indicated these as the most stable substitutions, in agreement with the Rietveld results. Furthermore, the changes observed in the PL behavior were associated with the presence of structural and electronic order–disorder effects, which caused a symmetry breaking and a local polarization in the crystal structure at medium range. This confirmed that the PL results are derived from a compromise between the presence of local defects (short-range disorder) and crystal lattice ordering (long-range order). Using Wulff's theorem, a simple model is suggested to determine the surface energies of α-Ag_2WO_4 crystals with atomic-level resolution, and the proposed computational technique was used to calculate the crystal morphologies at equilibrium. Potential particle shapes and their transformations in α-Ag_2WO_4 were evaluated by controlling the ratio between surface energy values of each face using this model. The substitution of Ag by Ni decreases the number of exposed surfaces and the shape change from hexagonal to faceted cubic in α-Ag_2WO_4 to α-$Ag_{2-2x}Ni_xWO_4$ (x = 0.08), respectively. This induces an increased number of shallow defects, improving the blue contributions in the PL profile.

The present findings provide a better understanding of the morphological, structural, and optical properties of novel α-$Ag_{2-2x}Ni_xWO_4$ microcrystals, and open the door for the modulation of their optical properties, and the development of novel devices based on new photonic materials.

Acknowledgements

The authors acknowledge the financial support of the following Brazilian research funding institutions: CDMF 2008/57872-1, FAPESP 2015/11917-8; 2013/07296-2; 2013/23995-8; 2014/04350-9; 2012/14468-1, CNPq 153299/2015-0; 147001/2013-7, INCTMN 573636/2008-7, CAPES and PNPD 1268069. J. A. and L. G. also acknowledge the financial support of the Spanish research funding projects: PrometeoII/2014/022 and ACOMP/2014/270 projects (Generalitat-Valenciana), Ministerio de Economia y Competitividad (CTQ2012-36253-C03-02) and Programa de Cooperación Científica con Iberoamerica (Brasil), of Ministerio de Educación (PHBP149-00020). We also acknowledge the Servei Informática, Universitat Jaume I for the generous allotment of computer time. We also wish to thank Júlio Sczancoski, Rorivaldo Camargo, Ana Lucia Oliveira, Maximo S. Li, and Madalena Tursi for their technical and scientific contributions.

Notes and references

1 J. Andres, L. Gracia, P. Gonzalez-Navarrete, V. M. Longo, W. Avansi Jr., D. P. Volanti, M. M. Ferrer, P. S. Lemos, F. A. La Porta, A. C. Hernandes and E. Longo, *Sci. Rep.*, 2014, **4**, 1–7.
2 L. S. Cavalcante, M. A. P. Almeida, W. Avansi Jr., R. L. Tranquilin, E. Longo, N. C. Batista, V. R. Mastelaro and M. S. Li, *Inorg. Chem.*, 2012, **51**, 10675–10687.
3 H. Chen and Y. Xu, *Appl. Surf. Sci.*, 2014, **319**, 319–323.
4 X. J. Cui, S. H. Yu, L. L. Li, L. Biao, H. B. Li, M. S. Mo and X. M. Liu, *Chem. – Eur. J.*, 2004, **10**, 218–223.
5 L. F. da Silva, A. C. Catto, W. Avansi Jr., L. S. Cavalcante, J. Andres, K. Aguir, V. R. Mastelaro and E. Longo, *Nanoscale*, 2014, **6**, 4058–4062.
6 Y. V. B. De Santana, J. E. C. Gomes, L. Matos, G. H. Cruvinel, A. Perrin, C. Perrin, J. Andres, J. A. Varela and E. Longo, *Nanomater. Nanotechnol.*, 2014, **4**, 1–10.
7 D. P. Dutta, A. Singh, A. Ballal and A. K. Tyagi, *Eur. J. Inorg. Chem.*, 2014, 5724–5732.
8 J. Li, C. Yu, C. Zheng, A. Etogo, Y. Xie, Y. Zhong and Y. Hu, *Mater. Res. Bull.*, 2015, **61**, 315–320.
9 E. Longo, L. S. Cavalcante, D. P. Volanti, A. F. Gouveia, V. M. Longo, J. A. Varela, M. O. Orlandi and J. Andres, *Sci. Rep.*, 2013, **3**, 1–4.
10 E. Longo, D. P. Volanti, V. M. Longo, L. Gracia, I. C. Nogueira, M. A. P. Almeida, A. N. Pinheiro, M. M. Ferrer, L. S. Cavalcante and J. Andres, *J. Phys. Chem. C*, 2014, **118**, 1229–1239.
11 V. M. Longo, C. C. De Foggi, M. M. Ferrer, A. F. Gouveia, R. S. Andre, W. Avansi, C. E. Vergani, A. L. Machado, J. Andres, L. S. Cavalcante, A. C. Hernandes and E. Longo, *J. Phys. Chem. A*, 2014, **118**, 5769–5778.
12 W. da Silva Pereira, J. Andres, L. Gracia, M. A. San-Miguel, E. Z. da Silva, E. Longo and V. M. Longo, *Phys. Chem. Chem. Phys.*, 2015, **17**, 5352–5359.
13 J. W. Tang and J. H. Ye, *J. Mater. Chem.*, 2005, **15**, 4246–4251.
14 M. Vafaeezadeh and M. Mahmoodi Hashemi, *RSC Adv.*, 2015, **5**, 31298–31302.
15 R. Zhang, H. Cui, X. Yang, H. Tang, H. Liu and Y. Li, *Micro Nano Lett.*, 2012, **7**, 1285–1288.
16 X.-Y. Zhang, J.-D. Wang, J.-K. Liu, X.-H. Yang and Y. Lu, *CrystEngComm*, 2015, **17**, 1129–1138.
17 R. A. Roca, J. C. Sczancoski, I. C. Nogueira, M. T. Fabbro, H. C. Alves, L. Gracia, L. P. S. Santos, C. P. de Sousa, G. E. da Luz Jr and J. Andres, *Catal. Scitechnol.*, 2015, **5**, 4091–4107.
18 I. M. Pinatti, I. C. Nogueira, W. S. Pereira, P. F. Pereira, R. F. Gonçalves, J. A. Varela, E. Longo and I. L. Rosa, *J. Chem. Soc., Dalton Trans.*, 2015, **44**, 17673–17685.
19 Z. Lin, J. Li, Z. Zheng, J. Yan, P. Liu, C. Wang and G. Yang, *New J. Chem.*, 2015, **9**, 7256–7265.
20 C.-X. Guo, B. Yu, J.-N. Xie and L.-N. He, *Green Chem.*, 2015, **17**, 474–479.
21 A. J. Vandenberg and C. A. H. Juffermans, *J. Appl. Crystallogr.*, 1982, **15**, 114–116.
22 X. Wang, C. Fu, P. Wang, H. Yu and J. Yu, *Nanotechnology*, 2013, **24**, 165602.

23 L. Cheng, Q. Shao, M. Shao, X. Wei and Z. Wu, *J. Phys. Chem. C*, 2009, **113**, 1764–1768.
24 M. Es-Saheb and S. M. Azhar, *Res. J. Appl. Sci., Eng. Technol.*, 2014, **7**, 3935–3947.
25 H. M. Rietveld, *J. Appl. Crystallogr.*, 1969, **2**, 65–71.
26 A. C. Larson and R. B. Von Dreele, *General Structure Analysis System*, New Mexico, 1994.
27 P. Skarstad and S. Geller, *Mater. Res. Bull.*, 1975, **10**, 791–799.
28 L. Finger, D. Cox and A. Jephcoat, *J. Appl. Crystallogr.*, 1994, **27**, 892–900.
29 G. Kresse and J. Furthmuller, *Phys. Rev. B: Condens. Matter Mater. Phys.*, 1996, **54**, 11169–11186.
30 G. Kresse and J. Hafner, *Phys. Rev. B: Condens. Matter Mater. Phys.*, 1993, **47**, 558–561.
31 G. Kresse and J. Hafner, *Phys. Rev. B: Condens. Matter Mater. Phys.*, 1994, **49**, 14251–14269.
32 J. P. Perdew, K. Burke and M. Ernzerhof, *Phys. Rev. Lett.*, 1997, **78**, 1396.
33 J. P. Perdew, J. A. Chevary, S. H. Vosko, K. A. Jackson, M. R. Pederson, D. J. Singh and C. Fiolhais, *Phys. Rev. B: Condens. Matter Mater. Phys.*, 1992, **46**, 6671–6687.
34 S. L. Dudarev, G. A. Botton, S. Y. Savrasov, C. J. Humphreys and A. P. Sutton, *Phys. Rev. B: Condens. Matter Mater. Phys.*, 1998, **57**, 1505–1509.
35 P. E. Blöchl, *Phys. Rev. B: Condens. Matter Mater. Phys.*, 1994, **50**, 17953–17979.
36 G. Kresse and D. Joubert, *Phys. Rev. B: Condens. Matter Mater. Phys.*, 1999, **59**, 1758–1775.
37 G. Wulff, *Z. Kristallogr.*, 1901, **34**, 449–530.
38 A. I. Rusanov, *Surf. Sci. Rep.*, 1996, **23**, 173–247.
39 D. Scopece, *J. Appl. Crystallogr.*, 2013, **46**, 811–816.
40 J. Andrés, L. Gracia, A. F. Gouveia, M. M. Ferrer and E. Longo, *Nanotechnology*, 2015, **26**, 405703.
41 K. Momma and F. Izumi, *J. Appl. Crystallogr.*, 2011, **44**, 1272–1276.
42 A. Turkovič, D. Fox, J. Scott, S. Geller and G. Ruse, *Mater. Res. Bull.*, 1977, **12**, 189–195.
43 G. M. Clark and W. P. Doyle, *Spectrochim. Acta*, 1966, **22**, 1441–1447.
44 S. M. Pourmortazavi, M. Rahimi-Nasrabadi, M. Khalilian-Shalamzari, M. M. Zahedi, S. S. Hajimirsadeghi and I. Omrani, *Appl. Surf. Sci.*, 2012, **263**, 745–752.
45 M. N. Mancheva, R. S. Iordanova, D. G. Klissurski, G. T. Tyuliev and B. N. Kunev, *J. Phys. Chem. C*, 2007, **111**, 1101–1104.
46 B. Li, M. Ai and Z. Xu, *Chem. Commun.*, 2010, **46**, 6267–6269.
47 T. George, S. Joseph and S. Mathew, *Pramana*, 2005, **65**, 793–799.
48 R. F. Goncalves, L. S. Cavalcante, I. C. Nogueira, E. Longo, M. J. Godinho, J. C. Sczancoski, V. R. Mastelaro, I. M. Pinatti, I. L. V. Rosa and A. P. A. Marques, *CrystEngComm*, 2015, **17**, 1654–1666.
49 R. F. Goncalves, M. J. Godinho, A. P. A. Marques, M. R. C. Santos, I. L. V. Rosa, E. Longo, M. S. Li, J. L. S. Sa and L. S. Cavalcante, *Electron. Mater. Lett.*, 2015, **11**, 193–197.
50 S. Kannan, K. Mohanraj and G. Sivakumar, *Spectrochim. Acta, Part A*, 2015, **138**, 92–98.
51 J. Wang, C. Zhang, Y. Liu, L. Li, S. Liu, G. Jia and S. Shen, *J. Alloys Compd.*, 2015, **633**, 395–400.
52 T. Sugimoto, *Adv. Colloid Interface Sci.*, 1987, **28**, 65–108.
53 M. L. Moreira, J. Andres, J. A. Varela and E. Longo, *Cryst. Growth Des.*, 2009, **9**, 833–839.
54 R. L. Penn and J. A. Soltis, *CrystEngComm*, 2014, **16**, 1409–1418.
55 G. Botelho, J. C. Sczancoski, J. Andres, L. Gracia and E. Longo, *J. Phys. Chem. C*, 2015, **119**, 6293–6306.
56 A. F. Gouveia, J. C. Sczancoski, M. M. Ferrer, A. S. Lima, M. R. M. C. Santos, M. S. Li, R. S. Santos, E. Longo and L. S. Cavalcante, *Inorg. Chem.*, 2014, **53**, 5589–5599.
57 G. Zhou, M. Lü, F. Gu, D. Xu and D. Yuan, *J. Cryst. Growth*, 2005, **276**, 577–582.
58 D. L. Wood and J. Tauc, *Phys. Rev. B: Solid State*, 1972, **5**, 3144–3151.
59 L. Tolvaj, K. Mitsui and D. Varga, *Wood Sci. Technol.*, 2011, **45**, 135–146.
60 D. W. Kim, I.-S. Cho, S. Lee, S.-T. Bae, S. S. Shin, G. S. Han, H. S. Jung and K. S. Hong, *J. Am. Ceram. Soc.*, 2010, **93**, 3867–3872.
61 V. M. Longo, E. Orhan, L. S. Cavalcante, S. L. Porto, J. W. M. Espinosa, J. A. Varela and E. Longo, *Chem. Phys.*, 2007, **334**, 180–188.
62 L. Gracia, A. Beltrán, D. Errandonea and J. Andrés, *Inorg. Chem.*, 2011, **51**, 1751–1759.
63 J. C. Sczancoski, L. S. Cavalcante, N. L. Marana, R. O. da Silva, R. L. Tranquilin, M. R. Joya, P. S. Pizani, J. A. Varela, J. R. Sambrano, M. S. Li, E. Longo and J. Andres, *Curr. Appl. Phys.*, 2010, **10**, 614–624.
64 G. Blasse and M. Wiegel, *J. Alloys Compd.*, 1995, **224**, 342–344.
65 M. V. Korzhik, V. B. Pavlenko, T. N. Timoschenko, V. A. Katchanov, A. V. Singovskii, A. N. Annenkov, V. A. Ligun, I. M. Solskii and J. P. Peigneux, *Phys. Status Solidi A*, 1996, **154**, 779–788.
66 E. V. Sokolenko, V. M. Zhukovskii, E. S. Buyanova and Y. A. Krasnobaev, *Inorg. Mater.*, 1998, **34**, 499–502.
67 B. M. Sinelnikov, E. V. Sokolenko and V. Y. Zvekov, *Inorg. Mater.*, 1996, **32**, 999–1001.
68 D. Chen, G. Z. Shen, K. B. Tang, H. G. Zheng and Y. T. Qian, *Mater. Res. Bull.*, 2003, **38**, 1783–1789.
69 R. Zhai, H. Wang, H. Yan and M. Yoshimura, *J. Cryst. Growth*, 2006, **289**, 647–651.
70 Z. Wang, G. Li, Z. Quan, D. Kong, X. Liu, M. Yu and J. Lin, *J. Nanosci. Nanotechnol.*, 2007, **7**, 602–609.
71 T. Liu, J. Chen and F. Yan, *J. Lumin.*, 2009, **129**, 101–104.
72 V. Longo, E. Orhan, L. Cavalcante, S. Porto, J. Espinosa, J. A. Varela and E. Longo, *Chem. Phys.*, 2007, **334**, 180–188.
73 M. L. Moreira, E. C. Paris, G. S. do Nascimento, V. M. Longo, J. R. Sambrano, V. R. Mastelaro, M. I. Bernardi, J. Andrés, J. A. Varela and E. Longo, *Acta Mater.*, 2009, **57**, 5174–5185.
74 E. Longo, E. Orhan, F. Pontes, C. Pinheiro, E. Leite, J. A. Varela, P. Pizani, T. Boschi, F. Lanciotti Jr and A. Beltran, *Phys. Rev. B: Condens. Matter Mater. Phys.*, 2004, **69**, 125115.
75 E. Orhan, J. A. Varela, A. Zenatti, M. Gurgel, F. Pontes, E. Leite, E. Longo, P. Pizani, A. Beltran and J. Andres, *Phys. Rev. B: Condens. Matter Mater. Phys.*, 2005, **71**, 085113.
76 F. A. Kroger and H. J. Vink, *Solid State Phys.*, 1956, **3**, 307–435.